

THE CHANDRA SURVEY OF THE COSMOS FIELD II: SOURCE DETECTION AND PHOTOMETRY

S. PUC CETTI¹, C. VIGNALI^{2,3}, N. CAPPELLUTI⁴, F. FIORE⁵, G. ZAMORANI³, T. L. ALDCROFT⁶, M. ELVIS⁶, R. GILLI³, T. MIYAJI^{7,8}, H. BRUNNER⁴, M. BRUSA⁴, F. CIVANO⁶, A. COMASTRI³, F. DAMIANI⁹, A. FRUSCIONE⁴, A. FINO GUENOV^{4,10}, A. M. KOEKEMOER¹¹, V. MAINIERI¹²

Draft version October 30, 2018

ABSTRACT

The *Chandra* COSMOS Survey (C-COSMOS) is a large, 1.8 Ms, *Chandra* program, that covers the central contiguous ~ 0.92 deg² of the COSMOS field. C-COSMOS is the result of a complex tiling, with every position being observed in up to six overlapping pointings (four overlapping pointings in most of the central ~ 0.45 deg² area with the best exposure, and two overlapping pointings in most of the surrounding area, covering an additional ~ 0.47 deg²). Therefore, the full exploitation of the C-COSMOS data requires a dedicated and accurate analysis focused on three main issues: 1) maximizing the sensitivity when the PSF changes strongly among different observations of the same source (from ~ 1 arcsec up to ~ 10 arcsec half power radius); 2) resolving close pairs; and 3) obtaining the best source localization and count rate. We present here our treatment of four key analysis items: source detection, localization, photometry, and survey sensitivity. Our final procedure consists of a two step procedure: (1) a wavelet detection algorithm, to find source candidates, (2) a maximum likelihood Point Spread Function fitting algorithm to evaluate the source count rates and the probability that each source candidate is a fluctuation of the background. We discuss the main characteristics of this procedure, that was the result of detailed comparisons between different detection algorithms and photometry tools, calibrated with extensive and dedicated simulations.

Subject headings: X-rays; Surveys

1. INTRODUCTION

It is well known that X-ray surveys are an extremely efficient tool to select Active Galactic Nuclei (AGN). For example in the *XMM-Newton* COSMOS survey, at the 0.5-2 keV limiting flux of $7 \cdot 10^{-16}$ erg s⁻¹ cm⁻², the AGN surface density is ~ 1000 deg⁻² (Hasinger et al. 2007, Cappelluti et al. 2007), a factor 2-4 greater than the AGN surface density in the most recent deep optical surveys, 250 deg⁻² in the COMBO-17 (Wolf et al. 2003) and 470 deg⁻² in VVDS Survey (Gavignaud et al. 2006). There are four main causes for the higher efficiency of X-ray surveys in finding AGN: 1) X-rays directly trace the super massive black hole (SMBH) accretion, while AGN

classification through optical line spectroscopy may suffer of incompleteness and/or misidentifications; 2) AGN are the dominant X-ray population. In fact most ($\sim 80\%$) of the X-ray sources AGN in deep and shallow surveys turn out to be AGN, unlike at optical wavelengths. 3) 0.5-10 keV X-rays (the typical *Chandra* and *XMM-Newton* energy band) are capable to penetrate column densities up to $\sim 10^{24}$ cm⁻², allowing the selection of moderately obscured AGN; 4) low luminosity AGN are difficult to select in optical surveys, because their light is diluted in the host galaxy emission.

So far *Chandra* and *XMM-Newton* have performed several deep, pencil beam, and shallower but wider surveys. Fig. 1 compares the flux limit and area coverage of the main *Chandra* and *XMM-Newton* surveys. This figure shows that *XMM-Newton* COSMOS and *Chandra*-COSMOS (C-COSMOS, Elvis et al. 2009, Paper I hereafter) surveys are the deepest surveys on large contiguous area. The coverage of larger areas at similar flux limits is today achieved only by serendipitous surveys using mostly not contiguous areas (see e.g., CHAMP, Kim et al. 2004a, 2004b, Green et al. 2004).

The Cosmic evolution survey (COSMOS, Scoville et al. 2007) is aimed at studying the interplay between the Large Scale Structure (LSS) in the Universe and the formation of galaxies, dark matter, and AGN. The COSMOS field is located near the equator (10h,+02degrees), covers ~ 2 square degrees as originally defined by the HST/ACS imaging (Koekemoer et al. 2007), with subsequent deep and extended multi-wavelength coverage overlapping this area. The size of COSMOS was chosen to sample LSS up to a linear size of about 50 Mpc h⁻¹ at $z \sim 1-2$, where AGN and star formation in galaxies are expected to peak. To study the role of AGN in galaxy evolution the X-ray data are fundamental. Therefore,

Electronic address: puccetti@asdc.asi.it

¹ ASI Science data Center, via Galileo Galilei, 00044 Frascati, Italy

² Dipartimento di Astronomia, Universita' di Bologna, via Ranzani 1, Bologna, Italy

³ INAF-Osservatorio Astronomico di Bologna, Via Ranzani 1, I-40127 Bologna, Italy

⁴ Max Planck Institut für extraterrestrische Physik, Giessenbachstrasse 1, D-85748 Garching bei München, Germany

⁵ INAF-OAR, via Frascati 33, Monteporzio, I00040, Italy

⁶ Harvard-Smithsonian Center for Astrophysics, 60 Garden St., Cambridge, MA 02138 USA

⁷ Instituto de Astronomía, Universidad Nacional Autónoma de México, Ensenada, México (mailing address: PO Box 439027, San Ysidro, CA, 92143-9027, USA)

⁸ Center for Astrophysics and Space Sciences, University of California San Diego, Code 0424, 9500 Gilman Drive, La Jolla, CA 92093, USA

⁹ INAF - Osservatorio Astronomico di Palermo, Piazza del Parlamento 1, I-90134 Palermo, Italy

¹⁰ University of Maryland, Baltimore County, 1000 Hilltop Circle, Baltimore, MD 21250, USA

¹¹ Space Telescope Science Institute 3700 San Martin Drive, Baltimore MD 21218 U.S.A.

¹² ESO, Karl-Schwarzschild-Strasse 2, D-85748 Garching, Germany

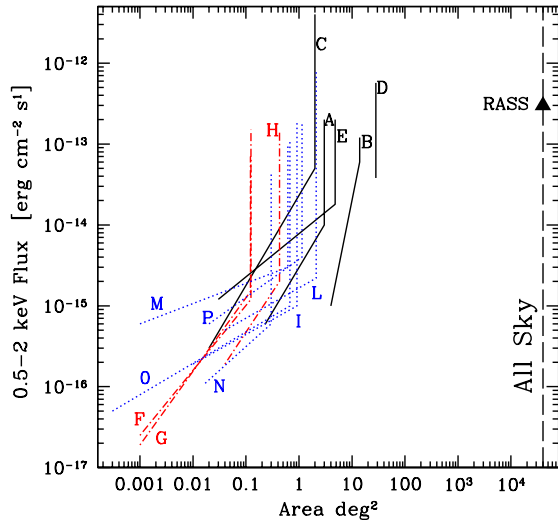


FIG. 1.— The 0.5-2 keV flux range vs. the area coverage for various surveys. The black solid lines represent few serendipitous surveys: Hellas2XMM (Baldi et al. 2002, symbol A), CHAMP (Kim et al. 2004a, 2004b, Green et al. 2004, symbol B), SEXSI (Harrison et al. 2003, symbol C), XMM-BSS (Della Ceca et al. 2004, symbol D), AXIS (Carrera et al. 2007, symbol E); the red dotted lines represent few deep pencil beam surveys: CDFN (Brandt et al. 2001, Alexander et al. 2003, symbol F), CDFS (Giacconi et al. 2001, Luo et al. 2008, symbol G), XMM-Newton Lockman Hole (Worsley et al. 2004, Brunner et al. 2008, symbol H); the blue dotted lines represent few wide shallow contiguous surveys: C-COSMOS (Elvis et al. 2009, symbol I), XMM-COSMOS (Hasinger et al. 2007, Cappelluti et al. 2007, 2009, symbol L), ELAIS-S1 (Puccetti et al. 2006, symbol M), E-CDF-S (Lehmer et al. 2005, symbol N), AEGIS-X (Laird et al. 2009, symbol O), SXDS (Ueda et al. 2008, symbol P). The black solid triangle represent the ROSAT all sky survey (RASS, Voges et al. 1999).

the central square degree of the COSMOS field has been the target of a *Chandra* ACIS-I, 1.8 Msec Very Large Program: the *Chandra*-COSMOS survey.

The C-COSMOS survey has a rather uniform effective exposure of ~ 160 ksec over a large area (~ 0.45 deg²), thus reaching ~ 3.5 times fainter fluxes than XMM-COSMOS in both 0.5-2 keV band and 2-7 keV band. This flux limit is below the threshold where starburst galaxies become common in X-rays. The sharp *Chandra* Point Spread Function (PSF) allows nearly unambiguous identification of optical counterparts (Civano et al. 2009, hereafter Paper III). *Chandra* secures the identifications of X-ray sources down to faint optical magnitude (i.e., $I \sim 26$), with only $\sim 2\%$ ambiguous identifications, significantly better than the $\sim 20\%$ ambiguous identifications in XMM-Newton (Brusa et al. 2007).

The C-COSMOS survey has a complex tiling (see Fig. 2) in comparison to other X-ray surveys, in which the overlapping areas of the single pointings are small and with similar PSFs (see e.g., the Extended Groth-Streep, AEGIS-X, Laird et al. 2009), or all the pointings are co-axial and nearly totally overlapping (see e.g., CDFS, Giacconi et al. 2001, Luo et al. 2008). In the C-COSMOS tiling, the pointings are strongly overlapping and not-coaxial. While this ensures a very uniform sensitivity over most of the field, each source is observed with up to six different PSFs, requiring the development of an

analysis procedure for data observed with this mixture of PSF. The procedures presented in this paper are aimed at optimizing (1) source detection, (2) localization, (3) photometry, and (4) survey sensitivity. We have made detailed comparisons between different detection algorithms and photometry tools, testing them extensively on simulated data. We furthermore validate our results by detailed inspections of each single source candidate. Our final analysis consists of a two main steps:

- 1 a wavelet detection algorithm, *PWDetect* (Damiani et al. 1997) is first used to find source candidates. This algorithm is optimized to cleanly separate nearby sources, to detect point-like sources on top of extended emission and to give the most accurate positions.
- 2 A maximum likelihood PSF fitting algorithm is then used to evaluate the source count rates and the probability that each source candidate is not a fluctuation of the background. We used the *emldetect* algorithm (Cappelluti et al. 2007 and references therein). *emldetect* works simultaneously with multiple overlapping pointings using PSFs appropriate to each one. This fitting method ensures accurate evaluation of the survey completeness and contamination, efficient deblending and good photometry for close pairs, which may be partly blended even at the *Chandra* resolution.

As a third step, we also performed aperture photometry for each candidate X-ray source using 50%, 90%, and 95% encircled count fractions, using the PSFs appropriate to each observation. The aperture photometry is also used to check the results. Aperture photometry is preferable in all cases where the systematic error introduced by PSF fitting are larger than the statistical errors, i.e., for bright sources (count rates ≥ 1 counts/ksec).

The survey sensitivity is limited by both the net (i.e., including vignetting) exposure time, and by the actual PSF with which a given region of the area is observed. The latter issue is particularly relevant for the C-COSMOS tiling. We have developed an algorithm that evaluates the survey sensitivity at each position on C-COSMOS using a parameterization of the *Chandra* ACIS-I PSF and taking into account the mixture of PSFs at each position. The resulting sensitivity maps have been compared and validated with extensive simulations.

The paper is organized as following: in Sect. 2 we briefly present the C-COSMOS observations and data reduction; we describe the simulations in Sect. 3; how they were used to select the most efficient detection algorithm and the final source characterization procedure is described in Sect. 4; the completeness and reliability are shown in Sect. 5; in Sect. 6 we apply this procedure to the observed data; in Sect. 7 we present the calculation of survey sensitivity, the sky-coverage, and X-ray number counts using the simulated data. Finally, in Sect. 8 we compare C-COSMOS to a similar *Chandra* survey, i.e., AEGIS-X, and in Sect. 9 we give our conclusion.

2. OBSERVATIONS AND DATA REDUCTION

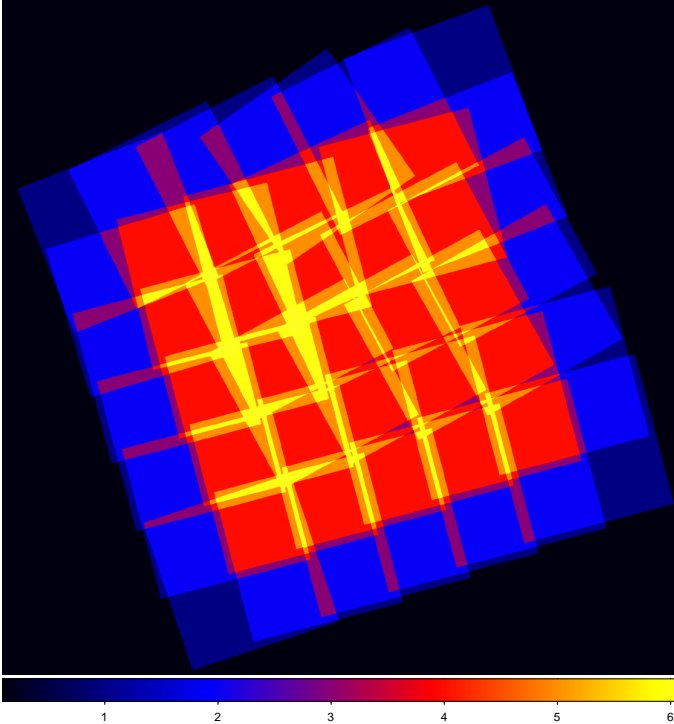


FIG. 2.— The final tiling of the C-COSMOS field, with a color scale showing the number of the ACIS-I overlapping pointings, as indicated in the color bar at the bottom of the figure.

We give here a brief description of the observations and data reduction. The full details are given in Paper I. The C-COSMOS field covers a contiguous area of $\sim 0.92 \text{ deg}^2$, centered at $10^h 00^m 18.91^s +02^\circ 10' 33.48''$, near the center of the full COSMOS field. The survey is made up of 36 different heavily overlapping ACIS-I pointings, each with a mean exposure of $\sim 50 \text{ ksec}$, for a total exposure of 1.8 Msec. Twelve of the 36 pointings were scheduled as two or more separate observations, with very similar roll-angles, thus resulting in 49 observations in total. Fig. 2 shows the number of ACIS-I pointings per pixel. Note that the central $\sim 0.45 \text{ deg}^2$ area is covered by four to six overlapping pointings, while most of the outer $\sim 0.47 \text{ deg}^2$ area is covered by one to two overlapping pointings. As an example, Fig. 3 shows the image of the same source observed in four overlapping fields at different off-axis angles.

The 49 observations were processed using the standard CIAO 3.4 software tools¹³ (Fruscione et al. 2006). Event files were cleaned of bad pixels, soft proton flares and cosmic-ray afterglows, and were brought to a common reference frame by matching the positions of bright X-ray sources with the optical position of bright ($18 < I < 23$), point-like optical counterparts. The systematic shifts between the X-ray and optical positions are $\Delta \text{RA} = 0.04''$ and $\Delta \text{DEC} = 0.25''$ (see Paper I). Observations with the same aim points and consistent roll-angles were merged together, producing 36 event files, one for each independent pointing.

The flux limits for source detection are influenced by three main factors: (1) net exposure time, (2) background per pixel, and (3) size of the source extraction region, which in turn depends on the size of the PSF

at the given position. The *Chandra* ACIS-I on-axis PSF has a spatial resolution of $0.5''$ FWHM, equivalent to $< 4\text{-}4.5 \text{ kpc}$ at any redshift, and permits observations of up to $\sim \text{Msec}$ to be photon limited. The adopted tiling produces a rather homogeneous exposure time over the C-COSMOS field (i.e., $\pm 12\%$ in the central $\sim 0.45 \text{ deg}^2$ area) and a uniform background. In the vignetting-corrected exposure time we clearly distinguish two main peaks at 80 and 160 ksec (see Fig. 7 of Paper I). Fig. 4 shows the fraction of the C-COSMOS area with a given background per square arcsec in the three analyzed energy bands: 0.5-7 keV (full band, F), 0.5-2 keV (soft band, S), and 2-7 keV (hard band, H). We see two main peaks at 0.07 and 0.14 counts/arcsec² in the F band and at 0.02 and 0.04 in the S band, corresponding to the two main peaks of the exposure time distribution. These peaks correspond to a level of ~ 2 and ~ 4 counts in the F band, and ~ 0.6 and ~ 1.2 counts in the S band over an area of 3 arcsec radius, a typical source detection region for off-axis angles less than 5-6 arcmin. Even the area with the largest exposure time has therefore relatively low background for point source detection; this is important for the detection of the faintest sources.

3. GENERATION OF SIMULATED DATA

Extensive simulations were performed in order to test various source detection schemes. The simulations were used (1) to test the reliability of the source position reconstruction, (2) to verify the count rate reconstruction, and (3) to assess and validate the level of significance of each detected source at each given detection threshold and thus to evaluate the level of completeness of the source list as a function of flux.

3.1. Creating the simulated input source catalog

In order to include realistic source clustering into the simulated data, we sampled particles from a COSMOS Mock galaxy catalog (V3.0) derived by Kitzbichler and White (2008). They made use of the Millennium Simulation (Springel et al. 2005), a very large simulation which follows the hierarchical growth of dark matter structures from redshift $z=127$ to the present. The simulation assumes the concordance ΛCDM cosmology and follows the trajectories of 2160^3 ($\sim 10^{10}$) particles in a periodic box $500 \text{ h}^{-1} \text{ Mpc}$ on a side, using a special reduced-memory version of the GADGET-2 code (Springel et al. 2001; Springel 2005). The formation and evolution of the galaxy population is simulated by using a semi-analytical model (Croton et al. 2006, De Lucia & Blaizot, 2007). We randomly selected 10000 mock galaxies per square degree in the ad hoc redshift range $0.4 < z < 0.9$ and i band magnitude range $17 < i < 26$. The selected random sources in this redshift-magnitude range show the same angular correlation function (ACF) as the S band XMM-COSMOS sources (Miyaji et al. 2007), as shown in Fig. 5, not taking into account that the clustering strength could depend on the survey flux limit (Plionis et al. 2008). The agreement between the ACF of the random sample and the XMM-COSMOS sample is good down to the 0.5 arcminute scale. Below 0.5 arcmin, the uncertainties in the S-band of the XMM-COSMOS ACF and the other X-ray ACF from literature (see e.g., the *Chandra* Deep Field South, D’Elia et al. 2004) are too large to allow them to be sensibly compared with the one

¹³ <http://cxc.harvard.edu/ciao/>

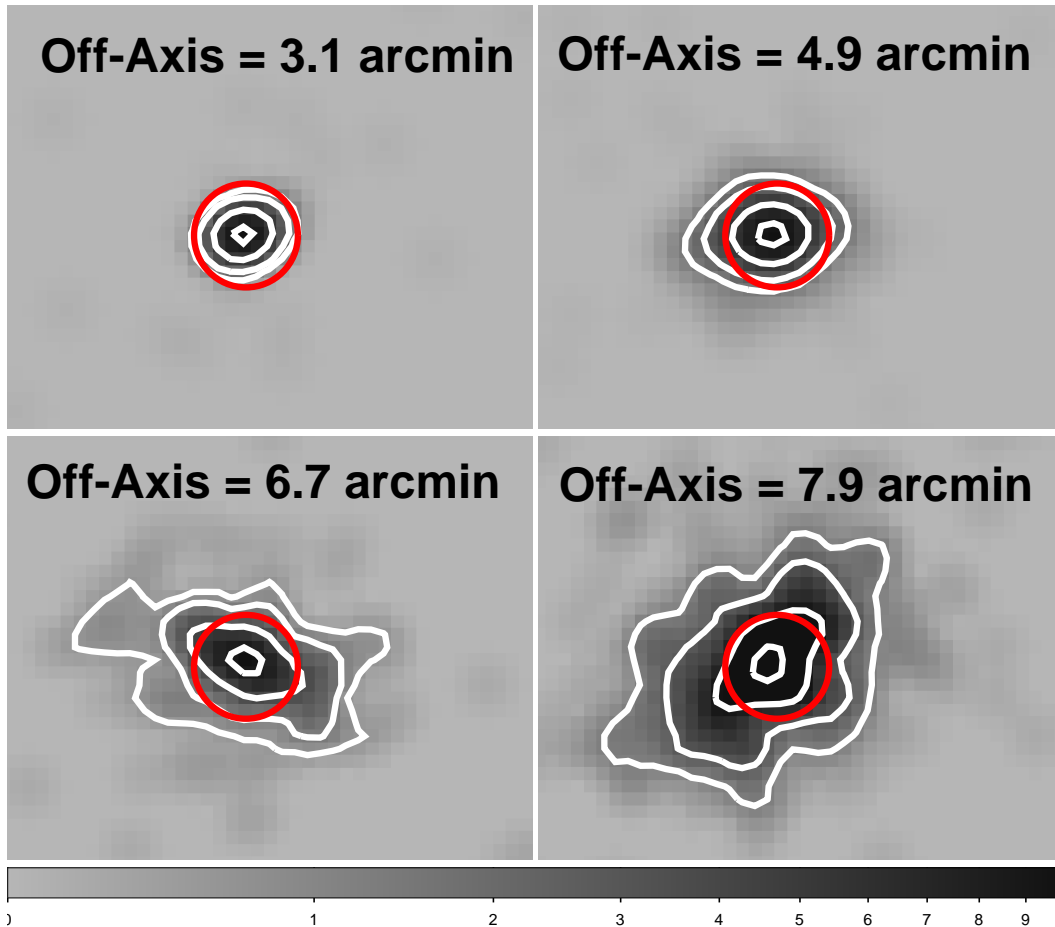


FIG. 3.— The image of the same source (i.e., source-id 50 in the C-COSMOS catalog presented in Paper I) observed in four overlapping fields at different off-axis angles. The contours are drawn at 90%, 50%, 25%, and 10% of the peak counts. The red circles centered on the position of the source have a radius of 2 arcsec.

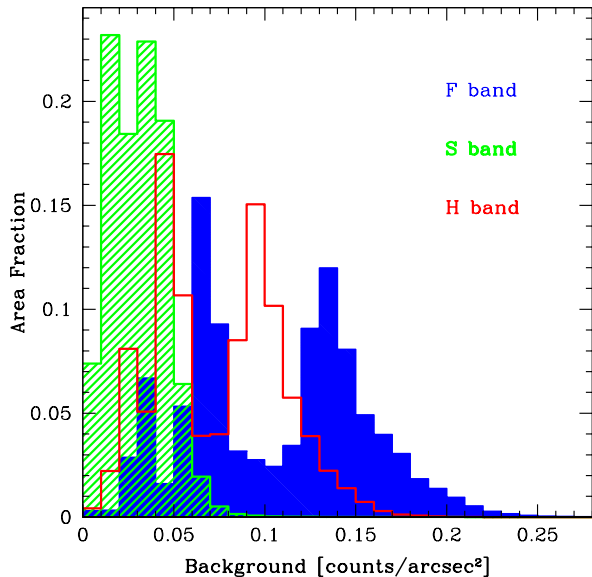


FIG. 4.— Area fraction for a given background per square arcsec in the F band (solid blue histogram), S band (dashed green histogram), and H band (empty red histogram).

we derive. Each simulated galaxy was then assigned an S band flux, randomly drawn from the number weighted $\log N - \log S$ relation of the AGN population synthesis model by Gilli et al. (2007). The corresponding minimum S band flux for the input particles was $\sim 3 \cdot 10^{-18}$ erg s $^{-1}$ cm $^{-2}$, which is a factor 100 below the detection limit of C-COSMOS. Hence background fluctuations due to unresolved faint sources are included in the simulations.

The S band flux of each source was then converted into an F band flux assuming a power-law spectrum with an energy index $\alpha_E = 0.4$ ¹⁴. The simulated sources cover a 3 deg 2 sky area, which is enough to completely enclose the COSMOS field.

3.2. Creating the simulated X-ray event files

Using the MARX simulator¹⁵ (version 4.2.1), we simulated a set of 49 *Chandra* ACIS-I pointings with the same exposure times, aim points, and roll-angles as the real C-COSMOS pointings (see Paper I). The simulated source list was fed into each simulated pointing and net source counts F recorded. This procedure returns 49 *Chandra* events files containing only source photons.

¹⁴ $f_E \propto E^{-\Gamma}$, with $\Gamma = \alpha_E + 1$

¹⁵ <http://space.mit.edu/CXC/MARX/>

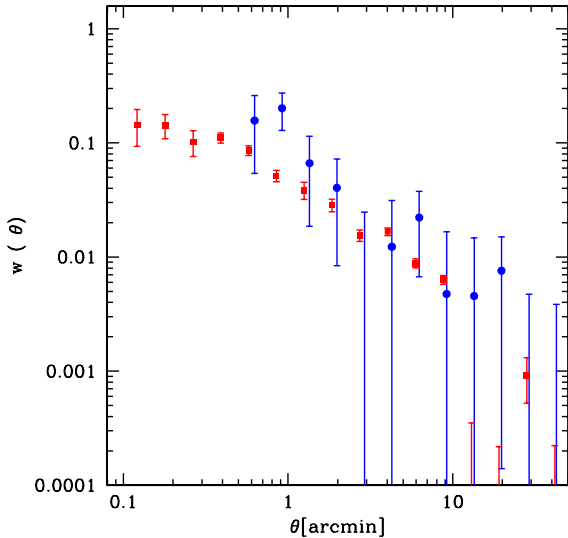


FIG. 5.— The ACF of the sources selected from the COSMOS Mock catalog for input to the C-COSMOS S band simulation (red squares) compared with that of XMM-COSMOS (S band, blue solid dots).

To include a background appropriate to each pointing we used the CXC compilation of blank sky fields¹⁶. These blank fields lie at high Galactic latitude, away from soft bright features such as the North Polar Spur, and have a median exposure of ~ 70 ks. Point-like and extended sources down to fluxes that would be detectable in each exposure have been excluded, and the individual exposures have been stacked into different blank sky files. We chose the stacked blank sky file appropriate for ACIS-I data at the epoch of our observations¹⁷, filtered to keep only photons detected in VFaint mode observations. This blank sky field has a total effective exposure of ~ 1.5 Msec.

We then extracted 49 background event files by randomly resampling the events out of the blank sky file scaling by the exposure time of each observation. Faint simulated sources with only a few counts would not be detected and increase the background level by $\sim 5\%$ at the depth of the blank sky observations. Since these faint, unresolved sources are already included in the blank sky files, in order to avoid counting them twice, we removed 5% of the photons in each background event file.

The background files were then reprojected to the coordinates of the real pointings by using the real aspect solution files, and then combined with the corresponding source event files. The final result is a set of 49 simulated ACIS-I fields that closely mirror the actual 49 observations.

4. CHOOSING THE C-COSMOS SOURCE DETECTION AND CHARACTERIZATION PROCEDURE

In order to fully exploit the large and deep C-COSMOS coverage a particular care had to be devoted to maximize

areal coverage and produce uniform depth; C-COSMOS used a complex tiling, with four overlapping pointings in most of the central ~ 0.45 deg² area with the best exposure, and two overlapping fields in most of the surrounding area, covering additional ~ 0.47 deg² (see Fig. 2). As a result, each source is observed at different off-axis angles, θ_i (i.e., the distance of the source position from the aim point in all overlapping fields), and thus with different PSFs. For some sources in the central area the number of different θ_i is as high as six. This mixture of PSFs requires addressing three main issues: (1) maximizing the sensitivity when the PSF changes so widely between different observations of the same source (from ~ 1 arcsec to ~ 10 arcsec half power radius); (2) maximizing the spatial resolution aimed to obtain the best source localization and the effective deblending; (3) obtaining accurate photometry, even in cases of partly blended sources. To solve these issues a dedicate analysis procedure was developed, and the simulations were used to determine and validate it.

We tested sliding cell and wavelet algorithms to find and locate source candidates, and both PSF fitting and aperture photometry. In particular, we compared the results obtained using the SAS *eboxdetect*¹⁸ and *emldetect*¹⁹ tasks, used for the XMM-COSMOS survey (Cappelluti et al. 2009), with those obtained using the *PWDelect* code (Damiani et al. 1997) and CIAO *wavdetect*²⁰ (Freeman et al. 2002). We compared *PWDelect* and CIAO *wavdetect* on a data subset including 8 ACIS-I fields and found consistent results. We adopt the *PWDelect* as the main wavelet algorithm because of its much faster processing time (i.e., factor of 40÷50) with respect to CIAO *wavdetect*.

4.1. *PWDelect*

The *PWDelect* code (Damiani et al. 1997) was originally developed for the analysis of ROSAT data, and was then adapted for the analysis of *Chandra* and XMM-Newton data. This method is particularly well suited for cases in which the PSF is varying across the image, as for *Chandra* images, since *PWDelect* is based on the wavelet transform (WT) of the X-ray image, i.e., a convolution of the image with a “generating wavelet” kernel, which depends on position and length scale, that is a free parameter. For the *Chandra* data, the length scale is varied from 0.35” to 16” in steps of $\sqrt{2}$. This choice spans the range from the smallest to the largest (for large θ_i) *Chandra* PSFs. Both radial and azimuthal PSF variations are accounted for by *PWDelect*, which first assumes a gaussian PSF and then corrects by a PSF shape factor, calibrated on both radial and azimuthal coordinates. *PWDelect* was run on each of the 36 event files with a low significance level of $\sim 10^{-3}$, to have entries with just 5 source counts (i.e., to pick up most of the input sources). The catalogs of source candidates from overlapping fields were then merged. The off-axis angle θ_i is recorded and the source position measured at the smallest θ_i (i.e., with the best PSF) is adopted as the reported source position. If a candidate is not detected in one or more of the overlapping fields, the count rate is computed at the position

¹⁶ <http://cxc.harvard.edu/contrib/maxim/acisbg/>

¹⁷ http://cxc.harvard.edu/contrib/maxim/acisbg/data/acisi_D_01236_bg_evt_010205.fits

¹⁸ <http://xmm.esac.esa.int/sas/8.0.0/eboxdetect/>

¹⁹ <http://xmm.esac.esa.int/sas/8.0.0/emldetect/>

²⁰ <http://asc.harvard.edu/ciao/ahelp/wavdetect.html>

of the source candidate and within a circle of radius R_i , corresponding to 90% of the encircled count fraction of the PSF ($f_{psf}^{21}=90\%$) at θ_i , as calibrated by the CXC²². Finally, a mean count rate, that is weighted by the count rate errors, is associated at each source. Analysis of the simulated data showed that all candidates with a wavelet size smaller than the PSF size and less than 5 counts are spurious detections. These were then excluded from the candidate catalogs.

4.2. EBOXDETECT and EMLDETECT

Both *eboxdetect* and *emldetect* are part of the XMM-Newton SAS package and are based on programs originally developed for the detection in ROSAT images (see e.g., Voges et al. 1999). *eboxdetect* is a standard sliding cell detection tool, which is run on each of the 49 single observations. *eboxdetect* produces a list of candidate sources down to a selected low significance level. The list of source candidates is then passed to the *emldetect* task. *emldetect* performs a simultaneous maximum likelihood PSF fitting for each candidate to all the images at each position (see e.g. Cappelluti et al. 2007 for more details on *eboxdetect* and *emldetect*). *eboxdetect* was run setting a low significance level (DET_ML=3 or $P_{random}=0.05$), to provide a list of source candidates to *emldetect*, that recognizes all possible significant sources.

emldetect has been adapted to run on *Chandra* data by replacing the *XMM-Newton* PSF library with the *Chandra* PSF library (see note 22), and to work with many different PSFs, simultaneously. The counts at each position were fitted using a model obtained by convolving the PSF at that position with a β model (Crudace, Hasinger and Schmitt 1988). The program interpolates over the calibration library of *Chandra* PSFs to find the most appropriate PSF at the position of each source in each observation. The more crowded is the field, the more candidates are fitted simultaneously. *emldetect* can provide both source positions and source count rates, or only source count rates using fixed source positions. We ran it fitting for both source positions and count rates. The best fit maximum likelihood, DET_ML, is related to the Poisson probability that a source candidate is a random fluctuation of the background (P_{random}):

$$DET_ML = -\ln(P_{random}) \quad (1)$$

Sources with low values of DET_ML, and correspondingly high values of P_{random} , are then likely to be background fluctuations.

4.3. Tests on simulations

We ran both detection algorithms on the simulated data. Catalogs of candidates were produced with both *eboxdetect* and *PWDetect*. These lists were visually inspected to identify obviously spurious detections on the wings of the *Chandra* PSF around bright sources, and near the edges of the ACIS-I chips. For both detection algorithms, the number of these clearly spurious detections is rather small in all three bands ($< 1 - 2\%$). These entries were deleted and the 'cleaned' lists used as input for the *emldetect* tool. The *emldetect* output catalog

²¹ f_{psf} indicates a fraction of the source counts distributed in a circular area, following the PSF shape.

²² <http://cxc.harvard.edu/caldb/>

TABLE 1
COMPARISON BETWEEN *eboxdetect+emldetect* AND *PWDetect*

Parameter 1	<i>eboxdetect+emldetect</i> 2	<i>PWDetect</i> 3
Comparison on source position:		
$\langle \Delta \text{ R.A.} \rangle^a$	$0.17'' \pm 0.16''$	$0.02'' \pm 0.15''$
$\langle \Delta \text{ Dec.} \rangle^a$	$-0.18'' \pm 0.15''$	$0.003'' \pm 0.15''$
$\Delta \text{ R.A. RMS}^b$	$0.32''$	$0.31''$
$\Delta \text{ Dec. RMS}^b$	$0.35''$	$0.34''$
Comparison on completeness of close pairs:		
% of missed pairs ^c	~ 75%	
Comparison on source photometry:		
$\langle \frac{F_x(F)}{F_{xI}(F)} \rangle^d$	0.97 ± 0.11	0.86 ± 0.12
$\langle \frac{F_x(S)}{F_{xI}(S)} \rangle^d$	1.00 ± 0.12	0.94 ± 0.14
$\langle \frac{F_x(H)}{F_{xI}(H)} \rangle^d$	1.05 ± 0.16	0.88 ± 0.17

NOTE. — Column (1) shows the parameters used to test the accuracy of source localization, the completeness on the recovery of close pairs, and the flux reconstruction of the two detection algorithm, which we used. Column (2) and (3) show the results for the *eboxdetect+emldetect* and the *PWDetect* algorithm, respectively.

^a The median and interquartile of the shifts between the R.A. or Dec. of the input sources and the R.A. or Dec of the detected sources, see also Fig. 6.

^b The RMS of the R.A. or Dec. shifts between input and detected positions, see also Fig. 6.

^c Percentage of the pairs with a separation smaller than 4 arcsec, that are missed in comparison to *PWDetect*, see also Fig. 7.

^d The median and interquartile of the ratio between the output detected and input simulated count rates in the F, S, and H band, see also Fig. 8.

was then cut at a conservative value of DET_ML=12 ($P_{random} < 6 \times 10^{-6}$), to ensure that the number of spurious detections in this catalog is practically zero, so that the results are not contaminated by spurious associations.

Matched catalogs between the input simulated catalog and the *emldetect* and *PWDetect* output catalogs were produced using two methods: (1) a conservative approach, using a fixed matching radius of 0.5 arcsec. This produces matched catalogs which probably miss a fraction of real associations, but are virtually free from spurious associations. (2) A maximum likelihood algorithm, to find the most probable association between an input source and an output detected source. We used the catalogs produced using the first method to study the accuracy of source localization and flux reconstruction, while we used the catalogs produced by the second method to study the completeness and reliability of the detection algorithms (see Sect. 5).

Table 1 summarizes the comparison of the results of the application of *eboxdetect+emldetect* and *PWDetect* on simulated data.

We first compared the best-fit source coordinates provided by *emldetect* and *PWDetect* with the input source positions (see Tab. 1). The RMS variations and the interquartile of the shifts are similar for the two detection algorithms; however, we find a small systematic median shift between input and detected R.A. and Dec. (see also Fig. 6) using *emldetect*. We conclude that *PWDetect*

provides positions of higher quality.

As a second step, we focussed on the ability of the detection algorithms to separate close pairs of sources in *Chandra* data, comparing the numbers of pairs found by *emldetect* and *PWDetect* (see Fig. 7 and Tab. 1). The two algorithms are equivalent for large ($>4''$) separations, but there is a deficiency in the number of pairs recovered by *emldetect* at small ($<4''$) separations. We verified that all the $\sim 75\%$ of the pairs with a separation smaller than 4 arcsec missed by *emldetect* are in the input source list, and not spuriously created by the splitting of a single source. Analysis of the *eboxdetect* candidate list and *emldetect* final list shows that the majority ($>70\%$) of these pairs are missed in the *emldetect* step, where the program finds a best fit including one significant source only, while the second falls below the detection threshold. We conclude that *PWDetect* is more efficient than *emldetect* at resolving close pairs with separations $<4''$ and greater than $\sim 1.8''$.

Finally we compared the *emldetect* and *PWDetect* best-fit count rates with the input count rates in the F, S, and H band (see Fig. 8 and Tab. 1). The *PWDetect* reconstructed count rates were systematically smaller than the input count rates by 10-20%. A similar problem was found by Puccetti et al. (2006) using a similar detection algorithm on *XMM-Newton* data. *emldetect* reconstructs much better the count rates in all the bands.

The accuracy of the count rate reconstruction of the *emldetect* algorithm is also good at all count rates, without any large systematic shifts, both at low count rates and at high count rates (see left panel of Fig. 9). The right panel of Fig. 9 shows the difference between the *emldetect* count rate and the input simulated count rate divided by the *emldetect* error on the count rate as a function of the *emldetect* count rate. We see that the distribution is approximately centered around zero for count rates smaller than ~ 0.5 counts/ksec, but becomes positive for larger count rates. This suggests that at high count rates, there is a not negligible systematic error in the *emldetect* count rate determination, due to the uncertainties in the PSF model becoming comparable to, or higher than, the statistical error. For this reason we also performed aperture photometry (see Sect. 6.4), which should be free from this systematic error.

4.3.1. Error on the positions

The source positional error is proportional to the PSF at the position of the source, and inversely proportional to the square root of the source number counts. We evaluated the errors on the positions by dividing the PSF_{radius} by (1) the square root of the total source plus background counts (T , $Pos_{Error} = PSF_{radius}/\sqrt{T}$) and (2) the square root of the net, background subtracted, source counts (C_s , $Pos_{Error} = PSF_{radius}/\sqrt{C_s}$). We used different PSF_{radius} , from 50% to 90% of the f_{psf} at the position of each source in the field where the source is detected at the smallest θ_i (i.e., with the best PSF).

These errors were then compared with the deviations between the X-ray positions and input positions in the simulations. Method (2) gave the best match using a PSF_{radius} corresponding to the 50% f_{psf} at the θ_i of each source, and the counts included in a circular region with the same radius. We used the $f_{psf} - \theta_i$ calibration

provided by CXC (see note 19). Larger PSF_{radii} provided implausibly large position errors for bright sources. Including background counts (method 1) produces too small errors for faint sources, where the background is not negligible. For ~ 60 sources with more than ~ 120 counts, the errors on RA and Dec are formally smaller than 0.07 arcsec (i.e., errors on source position smaller than 0.1 arcsec). In these cases the error on source position was conservatively set to 0.1 arcsec to account for possible small systematic errors in the astrometric corrections (see Sect. 2 and 4.3). Fig. 10 shows the distribution of the ratio between the deviation between the *PWDetect* positions and input positions and the X-ray error on the position evaluated as in method (2). The distributions in the three detection bands are similar and peak at a value of $\sim 0.7-0.8$. These distributions are compared with the expectation based on Gaussian statistics which peaks at unity. This comparison shows that the assumed errors on the positions, although very small, are, on average, somewhat larger than the deviation between input positions and detected positions. However, to account for small systematic errors in the astrometric corrections, which are not included in the input positions while they certainly affect the observed data, we use in the following the conservative errors on the positions computed as described above.

4.4. The final C-COSMOS source detection and characterization procedure

In summary, the comparison of the two methods *PWDetect* and *eboxdetect+emldetect* on the simulated C-COSMOS field shows that *PWDetect* is superior in separating closely spaced sources and in localizing sources, and relatively poor at photometry. Conversely, *emldetect* is poor at separating closely spaced sources, while it is good at estimating source reliability, completeness, and photometry. These results suggested the following source detection and characterization procedure:

- 1- *PWDetect* is run first with a low threshold to produce a catalog of source candidates, with the best localization;
- 2- this catalog of source candidates is used as input for *emldetect* which performs a PSF fitting to find the best fit maximum likelihood source count rate and the probability that each source candidate is a fluctuation of the background. In *emldetect* the coordinates used to fit each source are those provided by *PWDetect* for the most on-axis observation;
- 3- aperture photometry is used to get good photometry for bright sources.

This combined approach allows us to obtain both the best possible position determination and reliable photometry for all sources.

5. COMPLETENESS AND RELIABILITY

The threshold for source detection must be set by balancing *completeness* (the fraction of true sources detected, i.e., ratio between the number of the detected sources and the number of input simulated sources) versus *reliability* (one minus the fraction of spurious sources

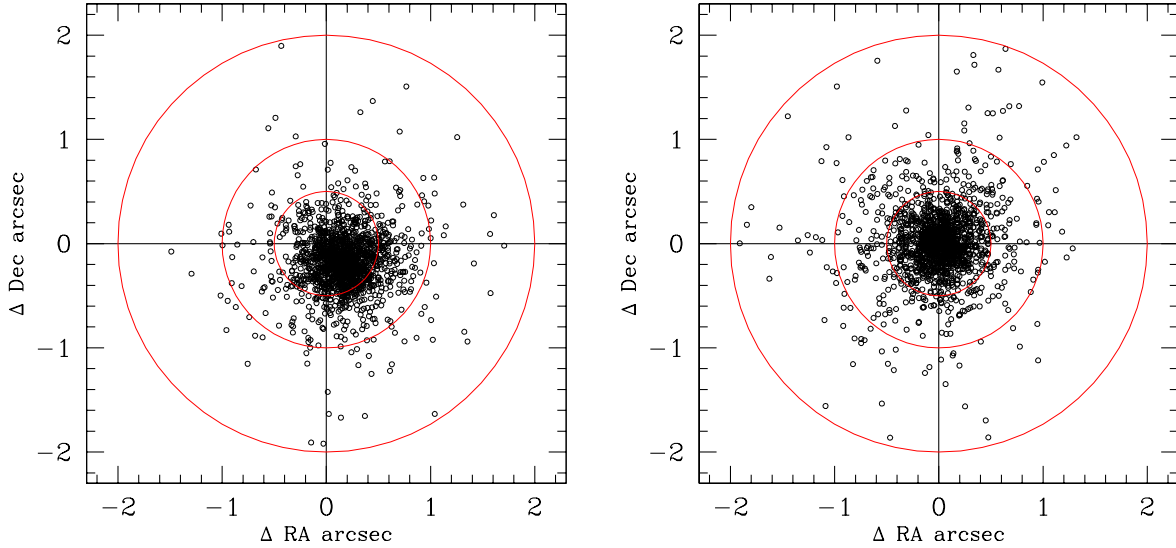


FIG. 6.— *Left panel*: shift between the input simulated source positions and the source positions by *emldetect* using a matching radius of 2 arcsec (black solid dots). The solid black lines represent the zero shifts. The red circles have a radius of 0.5, 1, and 2 arcsec, respectively. *Right panel*: shift between the input simulated source positions and the source positions by *PWDetect* using a matching radius of 2 arcsec (black solid dots). Symbols as in the left panel.

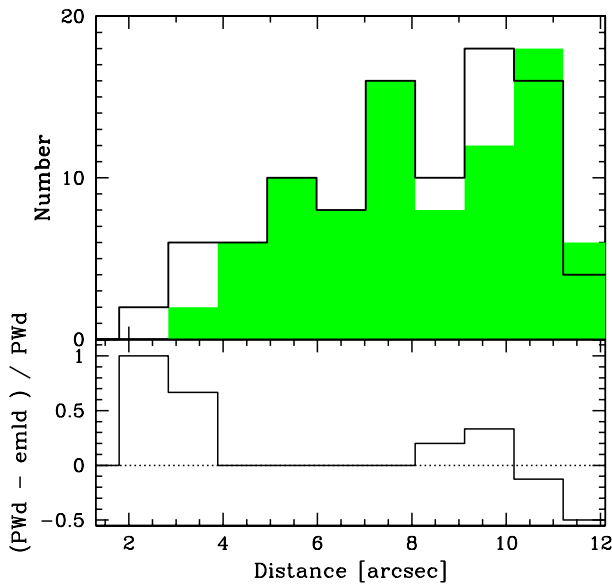


FIG. 7.— *Top panel*: number of pairs in the F band detected by *PWDetect* (black empty histogram) and *emldetect* (green solid histogram), as a function of the separation. *Bottom panel*: ratio between the difference between the number of pairs detected by *PWDetect* and *emldetect*, and the pairs detected by *PWDetect* as a function of the separation.

detected, i.e., one minus the ratio between the number of spurious sources and the number of input simulated sources). Our simulations allow us to choose a threshold which has a known completeness and reliability. The three panels of Fig. 11 show the completeness in the F, S, and H band as a function of the significance level for sources with at least 12 counts (solid lines) and 7 counts (dashed lines). The latter value refers to the counts of a typical source close to our flux limit, where we expect

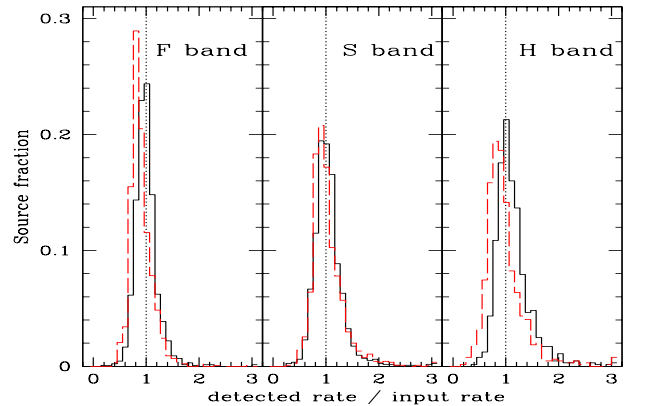


FIG. 8.— The *PWDetect* (red dashed histogram) and *emldetect* (solid black histogram) best fit count rates over the input count rates in the F (*left panel*), S (*center panel*), and H (*right panel*) band. The dotted vertical line corresponds to the exact match between the evaluated count rates and the input count rates. Note as the *emldetect* count rates are in good agreement with the input count rates.

a rather large incompleteness. The former value (12 counts) ensures significantly higher completeness. Fig. 11 also shows the reliability as a function of the significance levels for the same two cases. We chose a significance level of $2 \cdot 10^{-5}$ (or $\text{DET_ML}=10.8$), which represents a reasonable compromise between high completeness and high reliability. Higher significance levels give higher completeness but lower reliability. At the chosen threshold we have 87.5% and 68% (F band), 98.2% and 83% (S band), 86% and 67% (H band) completeness for sources with at least 12 and 7 counts, respectively. At the same significance level and the same counts limits, the reliability is $\sim 99.7\%$ for the three bands and both source count limits. This implies about 5, 4, and 3 spurious detections with ≥ 7 counts in the F, S, and H bands,

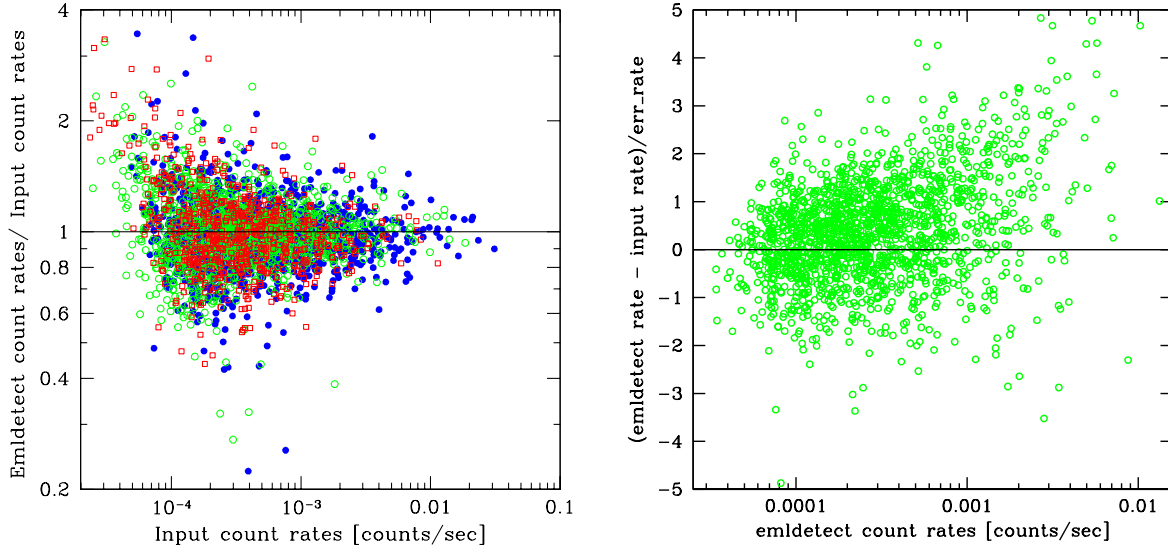


FIG. 9.— *Left panel:* The ratio between the best fit count rates obtained by *emldetect* and the input count rates as a function of the input count rates for the simulations in the F (blue solid circles), S (green open circles), and H (red open squares) band. The solid line is the exact match between the best fit count rates and the input count rates. *Right panel:* the difference between the *emldetect* count rate and the input count rate divided by the *emldetect* error on the count rate, as a function of the count rate for the sources detected in the S band.

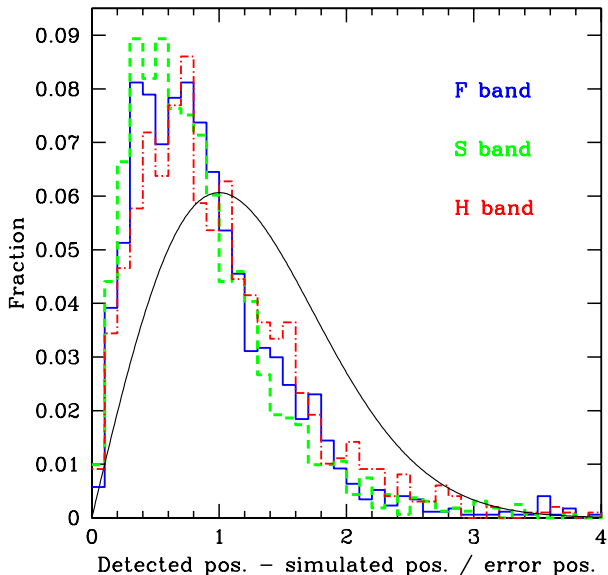


FIG. 10.— The distributions of the ratio between the deviation between detected positions by *PWDetect* and input positions and the X-ray error on the position for the simulations in three energy bands (blue: F band; green: S band; red: H band). The solid curve is the expectation based on Gaussian statistics.

respectively, and 3, 4, and 3 spurious detections with ≥ 12 counts in the same bands.

Fig. 12 shows the completeness for a significance level of $2 \cdot 10^{-5}$ as a function of the flux for the F, S, and H bands. Table 2 gives the flux limits corresponding to 4 completeness fractions in the F, S, and H bands.

We have also evaluated the completeness of the method in the detection of close pairs. Fig. 13 compares the number of pairs having one member with at least 7 and 12

TABLE 2
FLUX LIMIT AND COMPLETENESS

Completeness %	F(0.5-10 keV) erg cm $^{-2}$ s $^{-1}$	F(0.5-2 keV) erg cm $^{-2}$ s $^{-1}$	F(2-10 keV) erg cm $^{-2}$ s $^{-1}$
90	$4.1 \cdot 10^{-15}$	$1.1 \cdot 10^{-15}$	$7.8 \cdot 10^{-15}$
80	$3.1 \cdot 10^{-15}$	$9.4 \cdot 10^{-16}$	$6.1 \cdot 10^{-15}$
50	$1.7 \cdot 10^{-15}$	$4.5 \cdot 10^{-16}$	$2.9 \cdot 10^{-15}$
20	$1.1 \cdot 10^{-15}$	$3.3 \cdot 10^{-16}$	$2.0 \cdot 10^{-15}$

counts in the simulated data with the detected number of pairs. The number of pairs in the simulated data have been corrected dividing them by the square of the completeness expected at their counts thresholds (87.5% for the pairs with at least 12 counts and 68% for the pairs with at least 7 counts). In fact to correctly compare the number of pairs in the simulated data and the detected number of pairs, it is necessary to take into account that the detected number of pairs is not complete at the chosen significance level, and moreover that each pair must be corrected for the completeness of both sources in pair, that is the square of completeness. We see that at distances smaller than 5 arcsec, we miss between 50% and 70% of the pairs with at least 12 counts and between 70% and 80% of the pairs with more than 7 counts. The reason is that it is increasingly difficult to detect a faint (7 or 12 counts) source near a bright source, because of the wings of the PSF of the latter. Indeed, all pairs recovered have a counts ratio < 3 , while about 40% of the input pairs have a count ratio > 3 , none of which are detected in our analysis.

6. OBSERVED DATA: SOURCE DETECTION AND COUNT RATES

Source detection and characterization were performed on the real, observed, event files using the approach de-

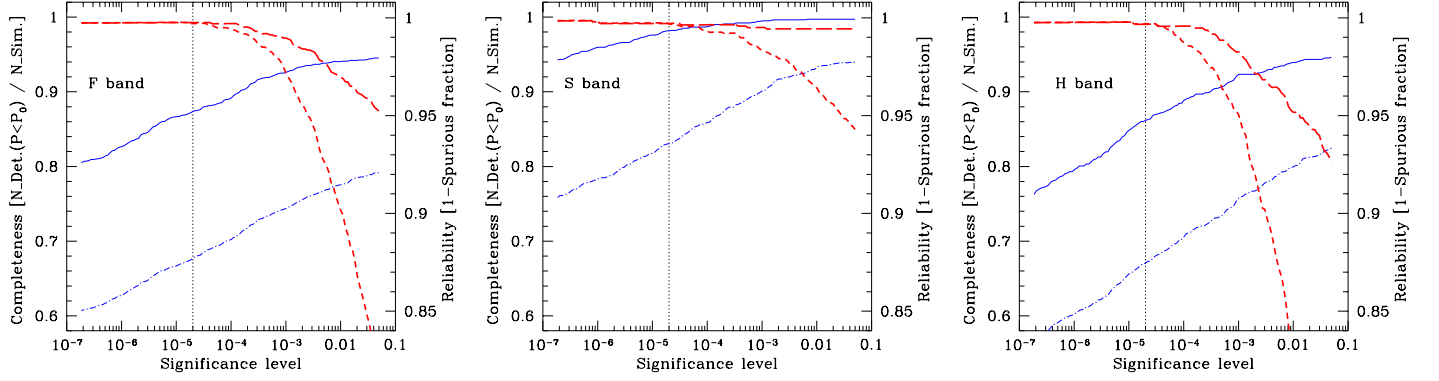


FIG. 11.— Completeness (solid and dot-short dashed lines, left y axis) and reliability (long dashed and short dashed lines, right y axis) as a function of the significance level for the simulations in the F (*left panel*), S (*center panel*) and H (*right panel*) band, for sources with at least 12 counts (solid and long dashed lines, respectively) and at least 7 counts (dot-short dashed and short dashed lines, respectively). The dotted vertical black lines indicate the chosen significance level of $2 \cdot 10^{-5}$.

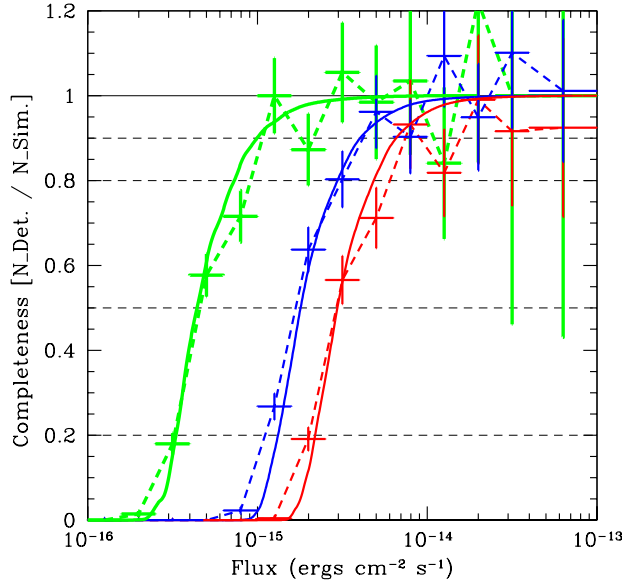


FIG. 12.— The crosses represent the completeness as a function of the flux at the chosen significance level of $2 \cdot 10^{-5}$, in F band (blue crosses), S band (green crosses), and H band (red crosses). The dashed lines connect the relative cross points. The solid lines represent the sky-coverage calculated as in Sect. 7.2 and normalized to the maximum sky-coverage. The horizontal black dashed and solid lines indicate 5 completeness fractions.

scribed in Sect. 4.4. The three energy bands, F, S, and H were used. The candidate catalogs produced by *PWDetect*, used as input for *emldetect* were cut at a low threshold of $\sim 10^{-3}$, corresponding to 5 counts. The number of *PWDetect* source candidates in each of the three bands was between 2500 and 3500. These lists were visually cleaned to identify obviously spurious detections on the wings of the *Chandra* PSF around bright sources and near the edges of the ACIS-I chips, following the same procedure adopted for the simulated data (see Sect. 4). As for the simulations, the number of clearly spurious detections is small in all three bands ($< 1 - 2\%$).

At the chosen probability (i.e. significance level $2 \cdot 10^{-5}$

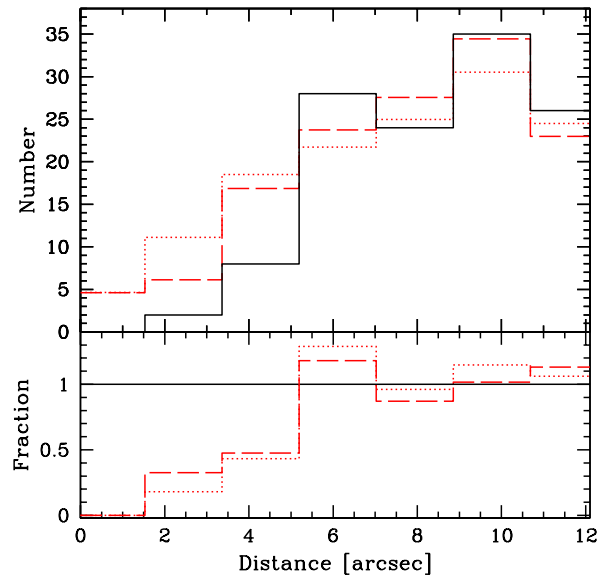


FIG. 13.— *Top panel*: the number of pairs in the F band detected by *PWDetect* (black solid histogram), compared to the number of pairs in the simulations having one member with at least 7 counts (dotted histogram) and 12 counts (dashed histogram) as a function of the separation. *Bottom panel*: ratio between the pairs detected by *PWDetect* and the number of pairs in the simulations with 7 or 12 counts as a function of the separation. In both panels the numbers of pairs in the simulations are corrected dividing them by the square of the completeness expected at their counts thresholds (see text).

or $\text{DET_ML}=10.8$), the number of spurious detections is presumably $\ll 12$ in the total catalog (i.e. F, S, and H band). The total catalog is obtained by the cross-correlation of the three single band (i.e. F, S, and H) catalogs, in this way the number of spurious sources in the single F, S, and H bands, evaluated by the detailed analysis of the simulations (see Sect. 5), are no longer independent. As a result the number of the total spurious sources is less than the sum of the spurious sources in each of three single bands.

6.1. Source position

Fig. 14 (left panel) shows the positional error, evaluated using the empirical technique described in Sect. 4.3.1, as a function of the off-axis angle. The notch in figure depends on the fact that at a fixed off-axis angle, the PSF_{radius} is \sim constant, while $\sqrt{C_s}$ is a discrete variable, since T are integer numbers and B are small. The error is typically less than ~ 0.5 arcsec at the smallest off-axis angles, $\theta_i < 2$ arcmin, and then increases to 1-2 arcsec for $\theta_i \geq 2$ arcmin. Most of the scatter at a given off-axis angle in this figure is due to the range of count rates in the sources. Fig. 14 (right panel) shows the positional error in the F band as a function of the source count rate in 4 off-axis bins. Both figures show that the quality of the data is good enough to provide positions with sub-arcsec accuracy, except for $\lesssim 12\%$ of F band sources (i.e., 202 sources), and for $\sim 13.5\%$ of the entire source catalog (see Paper I for more details). These small positional errors are the key to the high identification rate of the C-COSMOS sources with optical and infrared counterparts (Civano et al. 2009, Paper III).

6.2. Count rates

Vignetting corrected count rates for each source are obtained by dividing the best-fit counts derived from *emldetect* for each band and in each single field by the net exposure time, reduced by the vignetting at the position of each source, as in the exposure maps^{23,24}. The exposure maps are computed averaging over an area of 8 pixels to smooth out CCD gaps and cosmetic defects, and are weighted with an absorbed power-law spectral model with an energy index $\alpha_E = 0.4$ and the Galactic column density of the COSMOS field, $N_H = 2.7 \cdot 10^{20} \text{ cm}^{-2}$.

The errors on count rates at 68% confidence level were then computed using the equation:

$$\text{Error} = \frac{\sqrt{C_s + (1 + a) \cdot B}}{0.9 \cdot T_{\text{expo}}} \quad (2)$$

where C_s are the source net counts estimated by *emldetect*, corrected to an area including 90% of the PSF (see note 19), B are the background counts from the *emldetect* background maps (counts/pixel²) multiplied by a circular area of radius corresponding to $f_{\text{psf}}=90\%$ and T_{expo} is the vignetting corrected exposure time at the position of the source from the exposure maps. a is a parameter which accounts for the fact that the background at the source position is not known with infinite precision. $a = 1$ corresponds to the situation of a background area equal to the source extraction area, which for *Chandra* is always very small because of the very good PSF; $a = 0$ would correspond to assuming no uncertainty on the estimate of the average value of the background. Unfortunately *emldetect* provides neither the B errors, nor the information on the size of the region used to measure the background counts. Because of the way *emldetect* estimates the background counts, i.e. by a fit, using a sophisticated background modeling (Cappelluti et al. 2007), we are in an intermediate situation between the two extreme cases $a=0$ and $a=1$. For this reason, we chose to adopt $a=0.5$. This ensures that we are not under-estimating

the error on the background, even for sources close to problematic areas like the edge of the field or CCD gaps. We chose an area corresponding to $f_{\text{psf}}=90\%$, because this is the typical size of the area where *emldetect* works for relatively bright sources. We checked that the errors computed using Eq. 2 agree well with the errors evaluated from aperture photometry (Sect. 6.4).

Fig. 15 plots the signal-to-noise ratio²⁵ of each source as a function of DET_ML. Note the regular behavior of the signal-to-noise ratio, which increases smoothly and monotonically with increasing DET_ML, or with decreasing P_{random} (see Eq. 1), with a small dispersion around the correlation. The six diagonal black lines show the expectations computed for six values of the background in the detection cell, from 0.5 counts to 8 counts. This range is centered on ~ 4 counts, a value typical for the C-COSMOS survey (see Sect. 2), and accounts for two effects: a) the differences in exposure time and b) the difference sizes of the source extraction region as a function of the off-axis angle, due to the variation of the *Chandra* PSF with the off-axis angle. This range of background counts explains most of the observed dispersion in Fig. 15, especially for the faintest sources. For the brightest sources in the F band, the best fit DET_ML is somewhat smaller than expected based on the signal-to-noise ratio, even for the case of a background of 8 counts per detection cell. This can be explained if the fit of bright sources is performed over an area significantly larger than the 90% f_{psf} area, that so does not fully optimize the signal-to-noise ratio. This shift is smaller for the S band sources because of the smaller background in this band with respect to the F band.

6.3. Fluxes

The *emldetect* count rates (R) were converted to fluxes (F_x) using the formula: $F_x = R / (CF \cdot 10^{11})$, where CF is the energy conversion factor, that is evaluated by using spectra simulated through *Xspec*²⁶, including the appropriate on-axis response matrix and the chosen spectral models. We used energy conversion factors of 0.742 counts $\text{erg}^{-1} \text{ cm}^2$, 1.837 counts $\text{erg}^{-1} \text{ cm}^2$, and 0.381 counts $\text{erg}^{-1} \text{ cm}^2$ appropriate for a power-law spectrum with energy index $\alpha_E = 0.4$ and Galactic column density for the COSMOS field ($N_H = 2.7 \cdot 10^{20} \text{ cm}^{-2}$), to convert the F count rate into the 0.5-10 keV flux, the S count rate into the 0.5-2 keV flux, and the H count rate into the 2-10 keV flux, respectively. We extend the F and H bands up to 10 keV, to allow an easier comparison with the results of literature. The conversion factors are sensitive to the spectral shape: for $\alpha_E = 1$ they change by $\sim 40\%$ in the F band, by less than 5% in the S band and by less than 25% in the H band. For absorbed power-law spectra with $N_H = 10^{22} \text{ cm}^{-2}$ and $\alpha_E = 0.4$ or $\alpha_E = 1.0$, the conversion factors change by up to $\sim 46\%$ in the F band, by up to $\sim 17\%$ in the S band, and by up to $\sim 18\%$ in the H band (see Tab. 3). The conversion factor for the F band depends more strongly on the spectral shape because of the wider band.

6.4. Aperture photometry

²³ <http://hea-www.harvard.edu/~elvis/CCOSMOS.html>

²⁴ <http://irsa.ipac.caltech.edu/data/COSMOS/>

²⁵ Ratio between the source count rate and the error on the source count rate at 68% confidence level

²⁶ <http://xspec.gsfc.nasa.gov/>

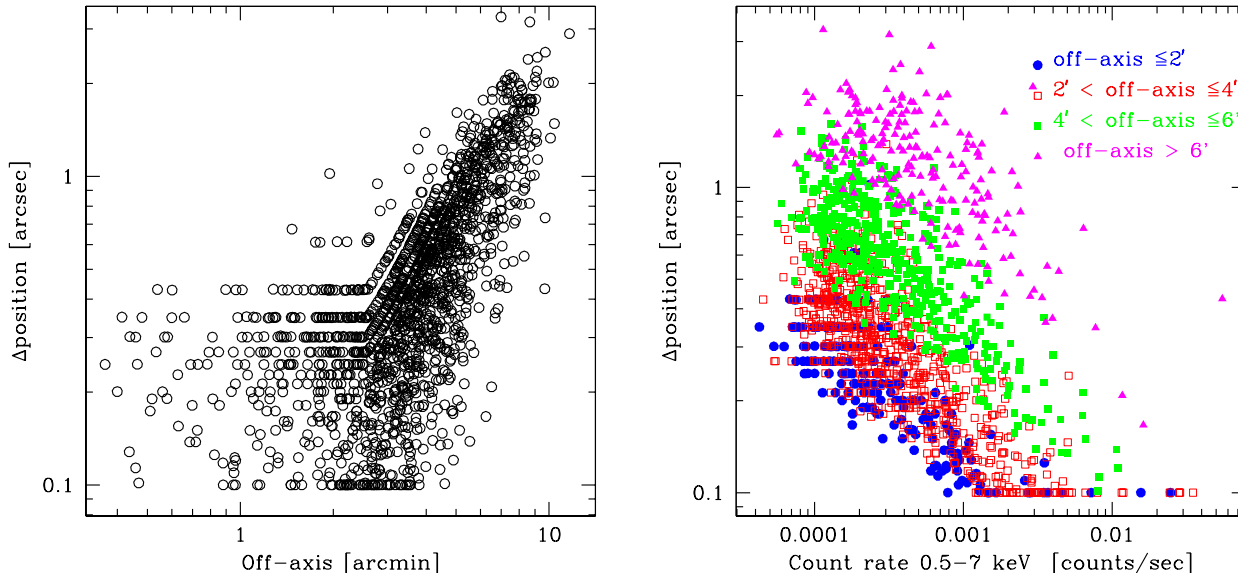


FIG. 14.— *Left panel:* The error on the source position as a function of the off-axis angle for sources detected in the F band. *Right panel:* the positional error in the F band as a function of the source count rate in 4 off-axis bins: filled circles = off-axis $<2'$; open squares = $2' < \text{off-axis} < 4'$; filled squares = $4' < \text{off-axis} < 6'$; filled triangles = off-axis $>6'$. The off-axis angle is the distance of the sources candidate position from the aim point of the pointing where the source position is measured with the best PSF (see Sect. 4.1).

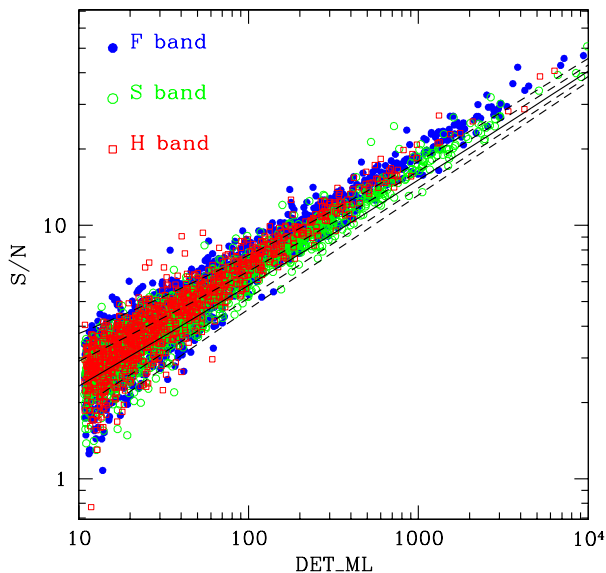


FIG. 15.— The signal-to-noise ratio of each source as a function of DET_ML. Filled circles = F sources; open circles = S sources; open squares = H sources. The six diagonal black lines correspond to the expectations assuming a background of 8, 4, 2, 1, and 0.5 counts in the detection cell, from top to bottom.

In addition to PSF fitting photometry, we have also performed standard aperture photometry on the sources included in the final *emldetect* catalog. We find an overall consistency between the two estimates, with the *emldetect* count rates slightly larger, less than 10 %, than the count rates by aperture photometry. For each source in the catalog, aperture photometry was performed in F, S,

TABLE 3
CONVERSION FACTORS FOR COUNT RATES TO FLUXES

α_E	N_H 10^{22} cm^{-2}	CF(F) ^a cts $\text{erg}^{-1} \text{ cm}^2$	CF(S) ^a cts $\text{erg}^{-1} \text{ cm}^2$	CF(H) ^a cts $\text{erg}^{-1} \text{ cm}^2$
0.4	0.027	0.742	1.837	0.381
1	0.027	1.042	1.759	0.474
0.4	1	0.508	2.12	0.361
1	1	0.712	2.151	0.447

^a energy conversion factor to convert the F count rate into the 0.5-10 keV flux (CF(F)), the S count rate into the 0.5-2 keV flux (CF(S)), and the H count rate into the 2-10 keV flux (CF(H)) using the formula $F_x = R / (\text{CF} \cdot 10^{11})$ and appropriate for a absorbed power-law spectra with the listed N_H and α_E .

and H band with the *yaxx* tool²⁷. The aperture photometry values are derived from event data for each individual *Chandra* observation, where a source is located. Then for sources being located in multiple observations, the aperture photometry is performed in each of the multiple observations, and the corresponding multiple aperture photometry values are combined to produce a single set of values, using the appropriate method shown in Tab. 4.

To extract source counts, circular regions of radii corresponding to 50%, 90%, and 95% f_{psf} , centered on each source location, are used for each observation, where the source is located. The radii are calculated using the off-axis and azimuthal angles of the source in each observation, and interpolating the circular f_{psf} table provided by the CXC calibration group to the nearest angles. Mean energies 2 keV, 1.2 keV, and 3.6 keV were chosen for the F, S, and H band, respectively. To extract background counts, annuli with the inner edge at the 95% f_{psf} radius plus 8 pixels, and with a width of 40 pixels

²⁷ <http://cxc.harvard.edu/contrib/yaxx/>

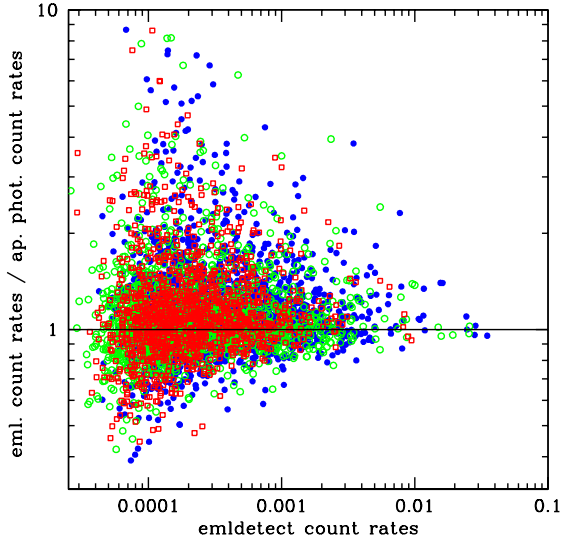


FIG. 16.— Ratio between the count rates evaluated by *emldetect* and count rates evaluated by the aperture photometry as a function of the *emldetect* count rates, for the F sources (blue filled dots), S sources (green open dots), and H sources (red open squares). The solid black line is the exact match between the *emldetect* count rates and the aperture photometry count rates.

are used. To limit contamination, all sources that overlap with the source or background regions are masked by using circular exclusion regions with the 95% f_{psf} radius. Exclusions can also come from the CCD edge, with an 8 pixel padding inward from the edge. Aperture fluxes for which the net source extraction area was less than 75% of the available area (i.e., the original circle prior to exclusions) are not given in the catalog.

Using the region described above, photometry was extracted using the CIAO tool *dmextract*. The source net counts were then corrected for the fraction of f_{psf} . *dmextract* was also run on the exposure maps with exactly the same regions in order to compute the vignetting corrected exposure times, that are needed to compute the source count rates.

Fig. 16 compares the count rates evaluated by *emldetect* with the count rates evaluated by the aperture photometry. The median and interquartile of the count rate ratios are 1.03 ± 0.16 , 1.08 ± 0.19 , 1.07 ± 0.18 in the S, H, and F band, respectively.

6.5. Upper limits

If a source is not detected in one band, we give the 90% upper limits to the source count rates and fluxes in this band. The upper limits are computed following as follows: if T is the total number of counts measured at the position of a source not satisfying our detection threshold, B are the expected background counts and X are the unknown counts from the source, the 90% upper limit on X ($X(90\%)$) can be defined as the number of counts $X(90\%)$ that gives 10% probability to observe T (or less) counts. Applying the Poisson probability distribution function, $X(90\%)$ is therefore obtained by iteratively solving for different X values the following equa-

tion:

$$0.1 = e^{-(X+B)} \sum_{i=0}^T \frac{(X+B)^i}{i!} \quad (3)$$

(see e.g., Narsky 2000). We collected the counts T both from a region of 5 arcsec radius and from the aperture photometry discussed in Section 6.5. The results were always statistically consistent with each other. The $X(90\%)$ upper limits derived with Eq. 3 do not take into account the statistical fluctuations on the expected number of background counts. In order to take the background fluctuations into consideration, we used the following procedure: if $\sigma(B)$ is the root mean square of B (e.g., $\sigma(B) = \sqrt{B}$ for large B), we estimated the 90% lower limit on B as $B(90\%) = B - 1.282 \cdot \sigma(B)$ ²⁸ and, as a consequence, the “correct” 90% upper limit on X becomes:

$$X_{corr}(90\%) \sim X(90\%) + 1.282 \cdot \sigma(B) \quad (4)$$

We used $X_{corr}(90\%)$ as upper limits for C-COSMOS sources. We also evaluated the upper limits following the method described in Kashyap et al. (2009). Comparing the upper limits obtained using the two methods, we found that our upper limits are generally more conservative (i.e., higher) than those which would be derived using the method by Kashyap et al. (2009).

7. SURVEY SENSITIVITY AND SKY-COVERAGE

7.1. Survey sensitivity

In X-ray observations the sensitivity, i.e., the flux limit, is not uniform in the field of view (FOV), due to two main reasons: (1) the variable size of the PSF, that determines the background counts that limit the source detection; and (2) the vignetting of effective area. In C-COSMOS, where we have used multiple overlapping pointings giving different PSFs and vignetting factors for each observation of each source, the problem of assessing the sensitivity at each position in the field of view is more complex than normal. To evaluate the C-COSMOS survey sensitivity, we have developed a dedicated procedure by adapting the analytical method, used for the easier case of the ELAS-S1 mosaic (Puccetti et al. 2006 and references therein), to the more complicated C-COSMOS mosaic. In this procedure, the full C-COSMOS field is divided into a grid of positions with spacing of 4 pixels, i.e., 2 arcsec. This bin size is a suitable balance between the spatial resolution in the C-COSMOS survey, and the ram memory required for computing the sensitivity maps. At each point of the 2 arcsec grid, we evaluated the minimum number of counts C_{min} needed to exceed the fluctuations of the background, assuming Poisson statistics with a significance level equal to that used for the catalog (i.e., $2 \cdot 10^{-5}$, see Sect. 6.1), according to the following formula:

$$P_{Poisson} = e^{-B} \sum_{k=C_{min}}^{\infty} \frac{B^k}{k!} = 2 \cdot 10^{-5} \quad (5)$$

²⁸ The value 1.282 is the value appropriate for the 90% probability (see e.g., Bevington P.R. and K. Robinson 1992). This approximate formula produces 90% limits which differ by $\sim 10\%$ (4%) from the exact estimate for values of $B = 5$ (10) in the extraction region, corresponding to 0.064 (0.128) cts/arcsec² (see Fig. 3).

TABLE 4
 MERGE METHODS

Parameter	Symbol	Merge method
exposure time corrected for the vignetting	T_{expo}	$\sum_i T_{expo_i}^1$
counts	T	$\sum_i T_i$
background counts	B	$\sum_i B_i$
net counts	C_s	$\sum_i C_{si}$
errors on counts	err_T	$\sqrt{\sum_i err_T_i^2}$
errors on background counts	err_B	$\sqrt{\sum_i err_B_i^2}$
errors on net counts	err_Cs	$\sqrt{\sum_i err_C_{si}^2}$
count rates	R	$\sum_i \frac{R_i \cdot T_{expo_i}}{T_{expo}}$
net count rates	R_s	$\sum_i \frac{R_{si} \cdot T_{expo_i}}{T_{expo}}$
count rate errors	err_R	$\sqrt{\frac{\sum_i err_R_i^2 \cdot T_{expo_i}}{T_{expo}}}$
net count rate errors	err_Rs	$\sqrt{\frac{\sum_i err_R_{si}^2 \cdot T_{expo_i}}{T_{expo}}}$

NOTE. — The index i indicates each of the observations where a source is located.

where B is the total background counts computed at the position of each point (P_j) of the grid by $B = \sum_{i=1}^n B_i$, where i runs from 1 to the number of overlapping fields at the position of each P_j and B_i are the background counts computed using the background map of each *Chandra* pointing covering the position, in a region centered at P_j and of radius R_i . R_i corresponds to a fixed value of f_{psf} , and is evaluated from the distance of P_j and the aim point of each single *Chandra* pointing covering the position, using the CXC calibration. We solved Eq. 5 iteratively to calculate C_{min} . The count rate limit, R_{lim} , at each point of the grid is then computed by:

$$R_{lim} = \frac{C_{min} - B}{f_{psf} \cdot T_{expo}} \quad (6)$$

where T_{expo} is the total, vignetting corrected, exposure time at each position of the grid, read from the merged C-COSMOS exposure map (see notes 20, 22).

Finally, the flux limits at each P_j are computed using the same conversion factor used for the real C-COSMOS sources. This procedure is applied to the S, H, and F bands to produce binned sensitivity maps.

7.2. Sky-coverage

The “sky-coverage” is the integral of the survey area covered down to a given flux limit, as a function of the flux in the sensitivity map. The solid lines in Fig. 12 are the normalized sky-coverages, computed using the procedure described above and adopting $f_{psf} = 0.5$. We studied how the sensitivity maps and the sky-coverage depend on the assumption on f_{psf} and found that they change less than few per cent for f_{psf} values up to 0.90. We also studied how the sensitivity maps change using different f_{psf} values at different off-axis angles where a single source is observed, finding again very little change. The reason for this behaviour is the relatively low background within each R_i , even at large off-axis angles.

A relatively large uncertainty in the sensitivity maps and sky coverage computation is instead, the unknown spectrum of the sources near the detection limit. The magnitude of this uncertainty depends on the width of the energy band, and therefore is largest in the F

band. To estimate the magnitude of the uncertainty, we calculated the sky coverage for power-law spectra with $\alpha_E = 1.0$, and for absorbed power-law spectra with $\alpha_E = 0.4$ or $\alpha_E = 1.0$ and $N_H = 10^{22} \text{ cm}^{-2}$, in addition to the baseline case ($\alpha_E = 0.4$, $N_H = 2.7 \cdot 10^{20} \text{ cm}^{-2}$; see Fig. 17). At the flux limits corresponding to 90% completeness (see Tab. 2) the deviations are less than 3%, $\sim 3\%$, and $\sim 16\%$ for the S, H, and F bands, respectively. This uncertainty related to the unknown spectrum of the sources becomes significant only at fluxes below the 50% completeness.

7.3. The $\log N - \log S$

We used the catalogs of the sources detected in the simulations in the S, H, and F bands, and the sky-coverage curves computed in Sect. 7.2 to obtain the number counts ($\log N - \log S$) of the sources detected in the simulations. We cut the catalogs in the S, H, and F band at a signal-to-noise ratio higher than 2, 2.5, and 2.8, respectively. These cuts are introduced because: (1) we do not correct for Eddington bias, which may be strong (up to 30-50%) at the lowest flux limits; (2) low signal-to-noise implies a large statistical uncertainty in the flux, which in turn would introduce a large uncertainty on the number counts at the lowest fluxes; (3) at the lowest fluxes, the sky-coverage is small, and the relative statistical and systematic errors are therefore large, again introducing large uncertainties in the number counts. We chose the signal-to-noise thresholds by requiring that the deviations between the $\log N - \log S$ computed from the detections and the input $\log N - \log S$ are smaller than 5%. The $\log N - \log S$ are shown in Fig. 18. The flux limits implied by the signal-to-noise thresholds are $\sim 2.3 \cdot 10^{-16}$, $\sim 1.6 \cdot 10^{-15}$, and $\sim 9.6 \cdot 10^{-16} \text{ erg s}^{-1} \text{ cm}^{-2}$ for the 0.5-2 keV, 2-10 keV, and 0.5-10 keV band, respectively. These flux limits are fully consistent with the flux limits of the $\log N - \log S$ derived from the observed data (see Paper I).

8. COMPARISON WITH AEGIS-X

Chandra was used to perform a survey somewhat similar to C-COSMOS in the Extended Groth-Streep

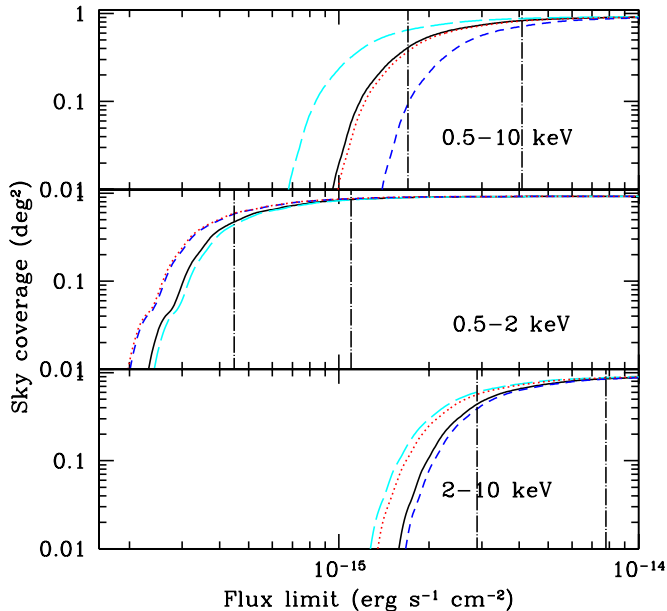


FIG. 17.— The sky-coverage calculated as in Sect. 7.2 for the 0.5–10 keV (*top panel*), 0.5–2 keV (*middle panel*), and 2–10 keV (*bottom panel*) band. The *black solid* lines represent the sky-coverages evaluated with the baseline model (i.e., power-law spectra with $\alpha_E = 0.4$ absorbed by Galactic $N_H = 2.7 \cdot 10^{20} \text{ cm}^{-2}$). The *cyan long-dashed* lines represent the sky-coverages for power-law spectra with $\alpha_E = 1$ absorbed by Galactic $N_H = 2.7 \cdot 10^{20} \text{ cm}^{-2}$. The *blue short-dashed* lines represent the sky-coverages for power-law spectra with $\alpha_E = 0.4$ absorbed by $N_H = 10^{22} \text{ cm}^{-2}$. The *red dotted* lines represent the sky-coverages for power-law spectra with $\alpha_E = 1$ absorbed by $N_H = 10^{22} \text{ cm}^{-2}$. The *black dot-long dashed* vertical lines represent the fluxes corresponding to the 90% and 50% completeness, respectively.

(AEGIS-X, Laird et al. 2009). The 1.6 Ms AEGIS-X survey is made of 8 ACIS-I pointings, each of a nominal 200 ksec exposure, with very little overlap, covering $\sim 0.67 \text{ deg}^2$. While the effective exposure time and area coverage are similar to C-COSMOS (see Fig. 19), the tiling is completely different. In C-COSMOS each source in the central area is observed at four to six different off-axis angles, while in AEGIS-X each source is observed only at one off-axis angle.

To compare the two surveys quantitatively, we cut the C-COSMOS catalog at the same significance level used for AEGIS-X (i.e., $4 \cdot 10^{-6}$ or $\text{DET_ML}=12.4$, Laird et al. 2009). We also recomputed the C-COSMOS sky-coverage using the same significance level. Fig. 19 compares the C-COSMOS sky-coverage to the AEGIS-X one computed without the Bayesian correction for the Eddington bias. The C-COSMOS sky-coverage has a significantly sharper drop toward lower fluxes than the AEGIS-X sky-coverage. This means that the sensitivity in C-COSMOS is more uniform over the field than in AEGIS-X, while the AEGIS-X tiling reaches fainter limiting fluxes than C-COSMOS. The estimated AEGIS-X flux limit in the S band is 50% deeper than C-COSMOS, while the flux limits in the H and F bands are about twice as deep as C-COSMOS, albeit in small areas. The deeper AEGIS-X flux limit in the H and F bands with respect to the S band depends on the higher internal background in these bands and on the smaller typical source extraction

regions in the areas of best sensitivity of AEGIS-X with respect to C-COSMOS. In fact, AEGIS-X has a PSF better than $\sim 1 \text{ arcsec}$ over an area of $\sim 0.15 \text{ deg}^2$, while the complex C-COSMOS tiling implies effective source extraction regions of radii of $\sim 3 \text{ arcsec}$ over most of the area.

The more characteristic flux limits corresponding to 90% completeness in the F, S, and H bands are similar in C-COSMOS and AEGIS-X, while the AEGIS-X flux limits corresponding to 50% completeness in the F, S, and H bands are lower than C-COSMOS by a factor 2–3 (see Tab. 5).

The more uniform sensitivity of C-COSMOS over the field reaches a higher source density (see Tab. 5).

C-COSMOS we estimate a slightly lower number of spurious sources at a higher significance level (i.e., $2 \cdot 10^{-5}$ vs. $4 \cdot 10^{-6}$, see Tab. 5), with respect to AEGIS-X survey. The number of spurious sources is roughly given by the product of the significance level times the number of independent detection cells in the field. The combination of different PSFs at each C-COSMOS position produces an effective source extraction region of $\sim 3 \text{ arcsec}$ radius, i.e., significantly wider than the Chandra PSF at off-axis angles smaller than 5–6 arcmin. This means that the number of independent cells per unit area is smaller in C-COSMOS than in AEGIS-X. In conclusion, the lower number of spurious detections in C-COSMOS with respect to AEGIS-X at a given significance level is due to the fact that each field is observed more than once at different off-axis angles and therefore with different PSFs.

9. CONCLUSION

The complex tiling of C-COSMOS survey required the development of a tailored multistep procedure to fully exploit the data. Detailed simulations were used to test different detection (sliding cell and wavelet) and photometry (PSF fitting and aperture photometry) algorithms. In particular, we compared the results obtained using the SAS *ebxdetect* and *emldetect* tasks, used for the XMM-COSMOS survey (Cappelluti et al. 2007, 2009), with those obtained using the *PWDetect* code (Damiani et al. 1997). Through these tests we selected a procedure consisting in first identifying source candidates using *PWDetect*, and then performing accurate PSF fitting photometry and evaluating aperture photometry for each source candidate. In this way we obtained subarcsec source localizations and accurate photometry even for partly blended sources.

We set a threshold for source detection to $P = 2 \cdot 10^{-5}$, which implies a completeness of 87.5% and 68% for sources with at least 12 and 7 F band counts, respectively, and 3 to 5 spurious detections in the F band at the same count limits, respectively.

We evaluated the survey sensitivity and the sky-coverage, through an analytical method, tuned using simulations. We then evaluated the $\log N - \log S$ of the detected sources in the simulations down to F, S, and H band flux limits of $F_x \sim 2.3 \cdot 10^{-16}$, $\sim 1.6 \cdot 10^{-15}$, and $\sim 9.6 \cdot 10^{-16} \text{ erg s}^{-1} \text{ cm}^{-2}$, respectively.

Finally we compared the C-COSMOS survey to the AEGIS-X survey, a *Chandra* survey with similar sky-coverage and total exposure time, but using non overlapping ACIS-I pointings. We found that the complex tiling of C-COSMOS helps in obtaining a contiguous area with

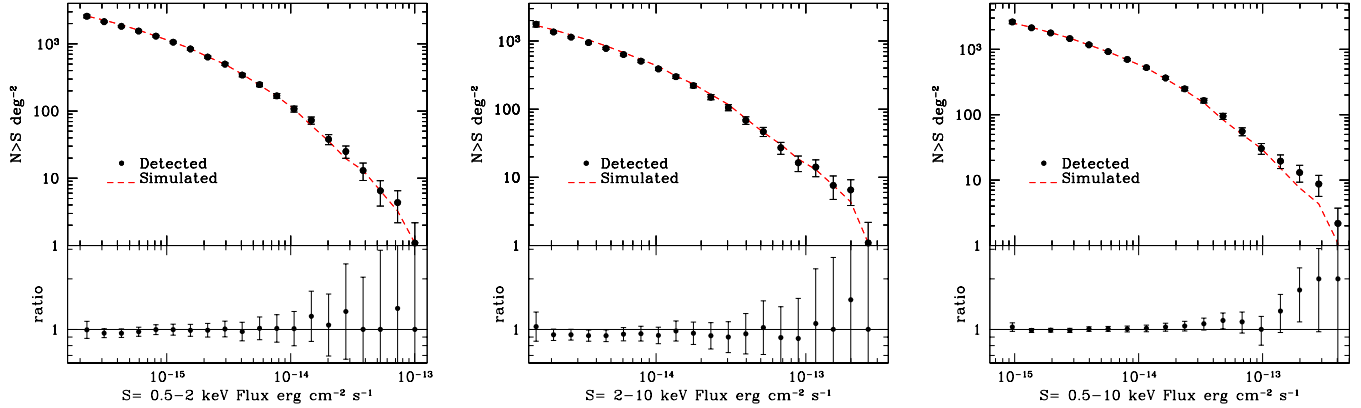


FIG. 18.— $\log N - \log S$ curves of the simulated sources (dashed red curves) compared with the $\log N - \log S$ curves of the sources detected in the simulations (black dots): *top left panel*: S band, *top middle panel*: 2-10 keV band, *top right panel*: 0.5-10 keV band. Ratio between $\log N - \log S$ curves of the simulated sources and the $\log N - \log S$ curves of the sources detected in the simulations: *bottom left panel*: 0.5-2 keV band, *bottom middle panel*: 2-10 keV band, *bottom right panel*: 0.5-10 keV band.

TABLE 5
COMPARISON BETWEEN C-COSMOS AND AEGIS-X

Parameter	units	C-COSMOS F	AEGIS-X F	C-COSMOS S	AEGIS-X S	C-COSMOS H	AEGIS-X H
90% Completeness ^a	$\text{erg cm}^{-2} \text{s}^{-1}$	$4.3 \cdot 10^{-15}$	$4.0 \cdot 10^{-15}$	$1.1 \cdot 10^{-15}$	$1.1 \cdot 10^{-15}$	$8.0 \cdot 10^{-15}$	$6.2 \cdot 10^{-15}$
50% Completeness ^a	$\text{erg cm}^{-2} \text{s}^{-1}$	$1.8 \cdot 10^{-15}$	$6 \cdot 10^{-16}$	$5.1 \cdot 10^{-16}$	$1.4 \cdot 10^{-16}$	$1.8 \cdot 10^{-15}$	$9 \cdot 10^{-16}$
observed source densities ^b	$\text{sources} \cdot \text{deg}^{-2}$	2110 ± 68	1830 ± 52	1700 ± 61	1550 ± 40	1320 ± 54	1110 ± 41
number of spurious sources ^c	sources	5	5	4	5	3	5
number of sources ^d	sources	1655	1221	1340	1032	1017	741

^a Completenesses are evaluated using a significance level of $4 \cdot 10^{-6}$.

^b The observed source densities are evaluated in the total AEGIS-X area, and in the central $\sim 0.45 \text{ deg}^2$ area in the C-COSMOS, which has similar effective exposure of the AEGIS-X survey, using a significance level of $4 \cdot 10^{-6}$.

^c In C-COSMOS the spurious sources are evaluated using a significance level of $2 \cdot 10^{-5}$ in the total field, for each band. For AEGIS-X Laird et al. (2009), using simulations, found 0.58 spurious sources per 200 ksec field per band using a significance level of $4 \cdot 10^{-6}$, corresponding to 5 spurious sources in the full AEGIS-X survey, each band.

^d Number of sources detected in each band in the total fields, using a significance level of $2 \cdot 10^{-5}$ and $4 \cdot 10^{-6}$ for C-COSMOS and AEGIS-X, respectively.

uniform sensitivity and somewhat higher source density. The overlap of several pointings with different PSF at the same position produces an effective source extraction region of ~ 3 arcsec radius, i.e., significantly wider than the Chandra PSF at off-axis angles smaller than 5-6 arcmin. This produces a number of independent detection cells per unit area smaller than in a single ACIS-I pointing survey like AEGIS-X, which in turn implies a smaller number of spurious sources at each given detection threshold.

This research has made use of data obtained from the *Chandra* Data Archive and software provided by the *Chandra X-ray Center* (CXC) in the application pack-

ages CIAO and Sherpa.

This work was supported in part by NASA *Chandra* grant number GO7-8136A (Martin Elvis, SAO, Francesca Civano, Marcella Brusa, Alexis Figonuenov), NASA contract NAS8-39073 (Chandra X-ray Center), and by NASA/ADP grant NNX07AT02G. In Italy this work is supported by ASI/INAF contracts I/023/05/0, I/024/05/0, I/026/07/0, I/088/06, and 2007/1.06.10.08, by PRIN/MUR grant 2006-02-5203. In Germany this project is supported by the Bundesministerium für Bildung und Forschung/Deutsches Zentrum für Luft und Raumfahrt and the Max Planck Society. In Mexico, this work is supported by CONACyT 83564 and PAPIIT IN110209.

REFERENCES

- Alexander, D. et al. 2003, 126, 539
 Baldi, A.; Molendi, S.; Comastri, A.; Fiore, F.; Matt, G.; Vignali, C. 2002, ApJ, 564, 190
 Bevington P.R. and K. Robinson “Data Reduction and error analysis for the physical sciences” 1992 by The McGraw-Hill Companies, Inc.
 Brandt, W.N., et al. 2001 AJ, 122, 2810
 Brunner, H.; Cappelluti, N.; Hasinger, G.; Barcons, X.; Fabian, A. C.; Mainieri, V.; Szokoly, G. 2008, A&A, 479, 283
 Brusa, M., et al. 2007, ApJS, 172, 353
 Cappelluti, N., et al. 2007, ApJS, 172, 341
 Cappelluti, N., et al. 2009, ApJ, accepted, arXiv:0901.2347
 Carrera, F. J. et al. 2007, *ibid.*, 469, 27
 Civano F., et al. 2009, in preparation, [Paper III]
 Croton, Darren J. et al. 2006, MNRAS, 365, 11
 Cruddace, R. G.; Hasinger, G. R.; Schmitt, J. H. 1988, ESOC, 28, 177
 Damiani, F., Maggio, A., Micela, G., & Sciortino, S. 1997, ApJ, 483, 350

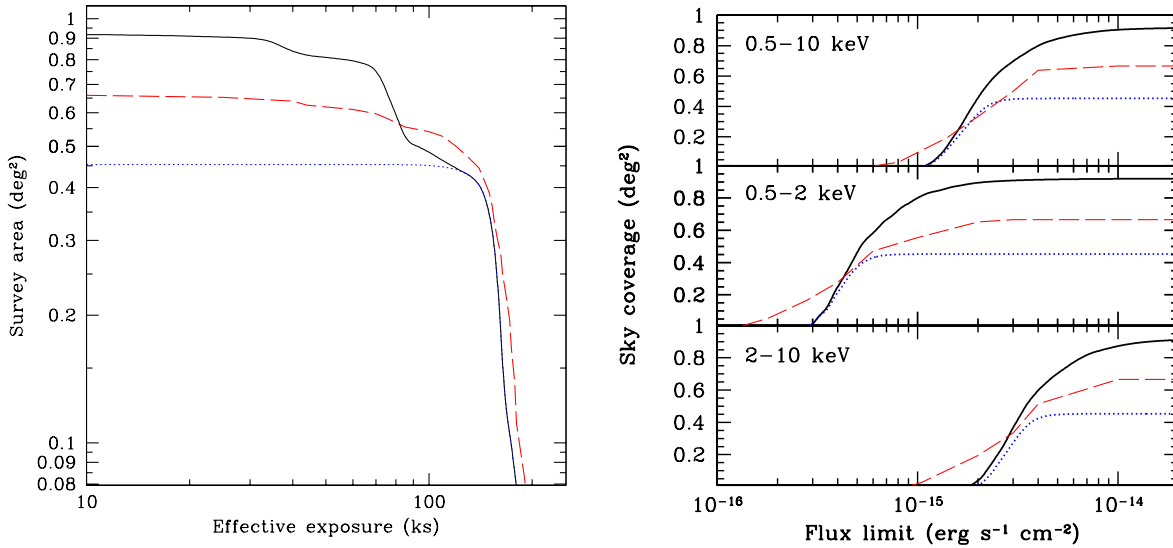


FIG. 19.— *Left panel:* the survey area coverage as a function of the effective (i.e., vignetting corrected) exposure time. *Right panel:* the sky-coverage calculated as in Sect. 7.2, using a significance level of $4 \cdot 10^{-6}$, in the 0.5-10 keV band (*upper panel*), in the 0.5-2 keV band (*middle panel*), and in the 2-10 keV band (*bottom panel*). In both panels, the solid black lines represent the total C-COSMOS survey, the dotted blue lines represent the central C-COSMOS $\sim 0.45 \text{ deg}^2$ area with the best exposure and the red dashed lines represent the AEGIS-X survey.

D'Elia, V.; Fiore, F.; Elvis, M.; Cappi, M.; Mathur, S.; Mazzotta, P.; Falco, E.; Cocchia, F. 2004, *A&A*, 422, 11
 Della Ceca, R. et al. 2004, *Å*, 428, 383
 De Lucia, Gabriella; Blaizot, Jérémy *MNRAS*, 375, 2
 Elvis, M., et al. 2009, *ApJS* 184, 158
 Freeman, P. E.; Kashyap, V.; Rosner, R.; Lamb, D. Q. 2002 *ApJS*, 138, 185
 Fruscione, A., et al. 2006, *Proc. SPIE*, 6270
 Gavignaud, I. et al. 2006, *Å*, 457, 79
 Giacconi, R., Rosati P., Tozzi P. et al. 2001, *ApJ*, 551, 664
 Gilli, R., Comastri, A., & Hasinger, G. 2007, *A&A*, 463, 79
 Green, P.J., et al. 2004, *ApJS*, 150, 43
 Harrison, Fiona A.; Eckart, Megan E.; Mao, Peter H.; Helfand, David J.; Stern, Daniel 2003, *ApJ*, 596, 944
 Hasinger, G. et al. 2007, *ApJS*, 172, 29
 Kashyap et al. 2009 <http://hea-www.harvard.edu/AstroStat/HEAD2008/WofCvkaWispzhd>
 Kim, D.-W. et al. 2004a, *ApJS*, 150, 19
 Kim, D.-W. et al. 2004b, *ApJ*, 600, 59
 Kitzbichler, M. G.; White, S. D. M. 2008, *MNRAS* 391, 1489
 Koekemoer, A. M. et al. 2007, *ApJS* 172, 196
 Laird, E. S., et al. 2008, *ApJS*, 180, 102

Lehmer, B. D. et al. 2005, *ApJS*, 161, 21
 Luo B., et al. 2008, *ApJS*, 179, 19
 Miyaji, T., et al. 2007, *ApJS*, 172, 396
 Narsky Ilya 2000, *Nucl.Instrum.Meth. A* 450, 444-455
 M. Plionis, M. Rovilos, S. Basilakos, I. Georgantopoulos, F. Bauer 2008, *ApJ*, 674, 5
 Puccetti, S., et al. 2006, *A&A*, 457, 501
 Scoville, N., et al. 2007, *ApJS*, 172, 1
 Springel, Volker; White, Martin; Hernquist, Lars 2001, *ApJ*, 549, 681
 Springel, V. 2005, *MNRAS*, 364, 1105
 Springel, Volker; White et al. 2005 *Nature*, 435, 629
 Ueda, Y. et al. 2008, *ApJS*, 179, 124
 Voges, W. et al. 1999, *A&A*, 349, 389
 Wilman, R. J.; Fabian, A. C. 1999, *MNRAS*, 309, 862
 Woffel, C.; Wisotzki, L.; Borch, A.; Dye, S.; Kleinheinrich, M.; Meisenheimer, K. 2003, *Å*, 408, 499
 Worsley M. A.; Fabian, A. C.; Barcons, X.; Mateos, S.; Hasinger, G.; Brunner, H. 2004, *MNRAS*, 352L, 28